Crystal-melt interfacial free energies and mobilities in fcc and bcc Fe

D. Y. Sun* and M. Asta
Department of Materials Science and Engineering, Northwestern University, Evanston, Illinois 60208, USA

J. J. Hoyt
Sandia National Laboratories, MS 1411, Albuquerque, New Mexico 87185, USA

(Received 16 December 2003; revised manuscript received 25 February 2004; published 10 May 2004)

Molecular-dynamics simulations have been used to compute thermodynamic and kinetic properties of the solid-liquid interface for both the fcc and bcc phases of Fe. Pure Fe was modeled using two different interatomic potentials of the embedded atom type as well as an effective pair potential. Free solidification simulations were used to determine the kinetic coefficient μ for the different models of pure Fe. The anisotropy of μ with respect to growth direction in the bcc phase is similar to that observed in fcc systems, namely $\mu_{100} > \mu_{110} \sim \mu_{111}$, and the kinetic coefficient of bcc is larger than μ for the fcc phase. The kinetic coefficient results are discussed in terms of a kinetic density-functional-theory-based model of crystal growth. In addition, results for solid-liquid interfacial free energies γ computed via the capillary fluctuation method, are summarized.

DOI: 10.1103/PhysRevB.69.174103 PACS number(s): 64.70.Dv, 68.08.−p, 81.30.Fb

I. INTRODUCTION

The magnitude and associated crystalline anisotropy of the solid-liquid interfacial free energy γ and mobility μ are known to be critical factors governing crystallization rates and growth morphologies accompanying crystal growth from the melt (e.g., Ref. 1). Due to significant challenges associated with direct experimental measurements,[2,3] much of the current theoretical understanding of crystal-melt interface properties has been derived from atomic-scale molecular-dynamics (MD) and Monte Carlo (MC) simulations (e.g., Ref. 4).

Two different methods, i.e., the cleaving method[5–7] and the capillary fluctuation method (CFM),[8] have been proposed to calculate the crystal-melt interfacial free energies directly from MD. The cleaving method was originally developed by Broughton and Gilmer in studies of the Lennard-Jones (LJ) system,[5] and later extended by Davidchack and Laird, who calculated γ for both the hard-sphere and Lennard-Jones models.[6,7] Hoyt, Asta, and Karma[8] developed an alternative approach for the calculation of γ, which relies on an analysis of the equilibrium capillary fluctuations in MD simulations for molecularly rough solid-liquid interfaces. The capillary fluctuation method was originally applied to studies of embedded-atom-method (EAM) metals[8–10] and alloys[11] and recently the approach was applied to the Lennard-Jones system by Morris and Song,[12] who obtained results consistent with those derived independently by the cleaving method.[7] As discussed elsewhere,[4,7] the cleaving technique typically yields more precise values of the interfacial free energy, whereas the CFM is more effective in resolving the small ($\sim$1%) anisotropy in γ found in typical solid-liquid systems.

The mobility of the solid-liquid interface is characterized by the so-called kinetic coefficient μ, which is defined as the constant of proportionality between the isothermal growth velocity and the interface undercooling. For calculating the kinetic coefficient from MD simulation, several alternative methods have been proposed as reviewed in Refs. 4 and 13. Kinetic coefficients have been calculated for the LJ system[14–19] and a number of fcc metals,[20–22] as well as for bcc sodium.[23,24] Simulations for LJ and fcc metals have demonstrated an important kinetic anisotropy given by $\mu_{100} > \mu_{110} \sim \mu_{111}$. From a phase field study of solidifcation in pure Ni, the kinetic anisotropy was shown to have important consequences for dendrite growth rates and morphologies at high undercooling.[25]

Until recently, detailed simulation studies of solid-liquid interfacial properties have focused primarily on systems whose equilibrium solid phase is the face centered cubic (fcc) crystal structure. Previous density-functional theory (DFT) calculations, experiments, and simulation-based nucleation studies have demonstrated a pronounced effect of crystal structure on γ. Specifically, in systems with stable fcc solids, formation of the body-centered-cubic (bcc) structure during crystallization has been frequently observed in experiments on deeply undercooled melts,[26–33] as well as in MD simulations[34] and DFT calculations for the LJ system.[35] The nucleation of metastable bcc crystals suggests lower values of γ for a bcc solid relative to fcc. Such observations motivated a recent study by the authors to examine the effect of bcc vs fcc crystal structure upon calculated values of γ in Fe.[36] In the current paper, we describe these calculations in further detail, and present an extension of this work to the study of the effect of crystal structure upon solid-liquid interface mobilities.

To date, only one MD simulation of μ has been performed for a bcc metal, namely, the work of Tymczak and Ray[23,24] who studied melting and crystallization of (100) solid-liquid interfaces in Na. To the best of our knowledge there has been, to date, no MD studies comparing results for μ and its anisotropy for fcc and bcc structures. Such a study is of significant interest within the context of experimental studies of dendrite growth rates in Fe-based alloys.[29,37] As discussed further below, significantly slower growth rates have been measured for dendrites of bcc crystals relative to

TABLE I. The calculated melting properties of bcc and fcc Fe for various interatomic potentials. The experimental melting point and latent heat are taken from Ref. 40; the volume change on melting is taken from Ref. 46.

	Structure	L (eV/atom)	T_m (K)	ΔV_{melt} (Å^3/atom)	ρ_{solid} (atom/Å^3)
Expt.	bcc	0.143	1811.0	0.45	0.0783
ABCH	bcc	0.218	2358.7±4.0	0.81	0.0784
ABCH	fcc	0.200	2251.0±6.0	0.60	0.0774
Pair	bcc	0.259	2311.8±3.0	1.28	0.0794
Pair	fcc	0.212	2202.0±7.0	0.84	0.0779
MH(SA)^2	bcc	0.162	1772.0±2.0	0.62	0.0801

fcc, an effect that has traditionally been attributed to lower values of the kinetic coefficient for bcc.

The remainder of the paper is organized as follows. The following section describes computational details, including the choice of interatomic potentials. Interfacial free energies calculated by the CFM are summarized in Sec. III, while results for isothermal crystallization and melting kinetics are presented in Sec. IV. In Sec. V, the results of the present MD studies are discussed in the context of theoretical models for the magnitude and crystalline anisotropy of μ. The conclusions drawn from this work are summarized in Sec. VI.

II. NUMERICAL PROCEDURES AND THEORETICAL BACKGROUND

A. Interatomic potentials

Two different many-body EAM potentials for Fe developed by Ackland *et al.*[38] and Mendelev *et al.*[39] are used in the present MD simulations. Hereafter, these potentials will be referred to by the initials of the authors: ABCH for Ackland *et al.* and MH(SA)^2 for Mendelev *et al.* Both potentials have the common EAM form for the energy of a configuration of N atoms:

$$E(\{\mathbf{R}_i\}) = \frac{1}{2}\sum_{i,j}^{N} \phi(\mathbf{R}_{ij}) + \sum_{i}^{N} U\left(\sum_{j}^{N} \rho(\mathbf{R}_{ij})\right), \qquad (1)$$

where $\mathbf{R}_{ij}$ is the distance between atoms i and j. In Eq. (1), ϕ is the pair interaction, while the term U gives rise to a many-body contribution to the energy of atom i that depends on its local environment, as characterized by the sum over the ''density'' function ρ. In both EAM potentials, the ϕ and ρ contributions were represented as sums of basis functions. In the ABCH model, U has the standard form of the tight-binding model, $U(\rho) = -\sqrt{\rho}$, while the MH(SA)^2 potential adopts the form $U(\rho) = -\sqrt{\rho} + \beta\rho^2$, with β a fitting parameter. The ABCH potential was derived by fitting to static properties of bcc Fe at zero temperature, including lattice constants, cohesive and vacancy-formation energies, and elastic moduli. MH(SA)^2 developed a more accurate potential by expanding the fitting database to include first-principles calculated interatomic forces in liquid Fe. In comparison to the original ABCH model, the MH(SA)^2 potential leads to much better agreement with experimental measurements for liquid structure factors and melting properties. With the ABCH potential, the melting temperature of bcc and fcc are very close, which is in agreement with phase diagram assessments (e.g., Refs. 40,41) and previous theoretical data[42,43]). By contrast, with the MH(SA)^2 potential, the fcc phase was found to be unstable at relatively low temperatures. In the present study we thus employ the ABCH to make direct comparisons between fcc and bcc crystal-melt interfacial properties, and employ the MH(SA)^2 to derive refined values for bcc interfaces.

In addition to calculations based on the EAM potential described above, we examine also a simpler ''effective'' pair potential.[44] By comparing to EAM, we can thus investigate the role of many-body interactions and the effect of the detailed form of the potential on calculated interfacial properties. The effective pair potential is obtained from the many-body ABCH interatomic potential by Taylor expanding the nonlinear density dependence of the embedding function to first order, employing the formula given by Carlsson:[44]

$$\Phi(\{\mathbf{R}_i\}) = \phi(\mathbf{R}_{ij}) + 2U'(\bar{\rho})\rho(\mathbf{R}_{ij}). \qquad (2)$$

In Eq. (2), $\bar{\rho}$ is a reference electron density, and U' denotes a derivative of the embedding function with respect to ρ. In the present work $\bar{\rho}$ is taken as the average of the bcc solid and liquid densities at the melting point. In our earlier paper,[36] $\Phi(\{\mathbf{R}_i\})$ was compared to a LJ potential with the same equilibrium spacing and well depth, and was shown to be significantly shorter in range, and less repulsive at short distances.

B. Melting properties and interfacial free energies

Melting temperatures were first determined for each potential by employing a slight modification of the MD coexistence technique[45] as described in detail in our previous paper.[13] Refined estimates were also derived by fitting interface velocity versus undercooling data obtained from MD simulations of crystal growth (see below). Calculated melting temperatures T_M, as well as latent heats L, volume change on melting (ΔV_{melt}), and solid densities at T_M are listed in Table I. The error quoted for T_M reflects primarily the uncertainty originating from finite system size effects, since the statistical uncertainties were estimated to be relatively small. The finite-size effect was estimated through

the melting temperature spanned for different size MD cells. For the bcc phase, the latent heat and melting temperature calculated by the MH(SA)^2 potential are much closer to the experimental data, i.e., $T_M = 1772.0 \pm 2.0$ K and $L = 0.162$ eV/atom for MH(SA)^2, while the experimental values are 1811.0 K and 0.143 eV/atom for the melting temperature and latent heat, respectively.[40] All the potentials overestimate the volume difference between solid and liquid at T_M for the bcc phase. The experimental value of the volume change on melting is 0.45 Å^3/atom,[46] the MH(SA)^2 potential overestimates the expansion by about 60%, and the ABCH and effective pair potentials yield values 2 and 3 times higher, respectively. For the fcc phase the melting point at zero pressure extrapolated from phase diagram assessments is estimated to be 1800.8 K (e.g., Ref. 41), which is lower than the melting point for the bcc phase by roughly 0.6%. Similarly, calculations based on a model that combines a nearly free-electron treatment of the *s* electrons and a tight-binding description of *d* electrons also predicts a zero-pressure melting temperature for fcc 50 K lower than bcc,[42] in good agreement with the present results obtained with the ABCH potential. Interestingly, the effective pair potential gives a very similar melting temperature as the many-body ABCH model, i.e., the T_M changes by only 2%. However, the latent heat differs by approximately 20% and volume changes on melting are roughly 30% different.

C. Interfacial free energies

Solid-liquid interfacial free energies were calculated by employing the capillary fluctuation method. The primary advantage of this method is that it measures directly the interface stiffness, which is an order of magnitude more anisotropic than the interface free energy itself. As discussed by Hoyt *et al.*,[8] the method thus facilitates precise calculations of the anisotropy. The method is based on the capillary fluctuation spectrum of a quasi-one-dimensional interface:

$$\langle |A(k)|^2 \rangle = \frac{k_B T}{bW(\gamma + \gamma'')k^2}, \tag{3}$$

where $A(k)$ is the Fourier transform of the interface height profile and angular brackets correspond to equilibrium values. W and b, with $b \ll W$, denote the length and thickness of the solid-liquid boundary, and $k_B T$ is Boltzmann's constant times the temperature. The term $\gamma + \gamma''$ corresponds to the interface stiffness, where γ'' is the second derivative of γ as a function of the angle of the local interface normal relative to its average orientation.

The size and geometries of the simulation cells, the equilibration procedure, and the method for locating the position of the solid-liquid interface have been described in detail in our earlier paper.[36] A total of six CFM cell orientations have been investigated in the present study. The large number of orientations is used to test, for bcc systems, the accuracy of the cubic harmonic expansion describing the orientation dependence of γ.

TABLE II. Values for the kinetic coefficient derived from the free solidification method for different interface orientations, system sizes, and potentials.

Orientation	Size	Potential	μ (cm/s K)
bcc(100)	(10×10×100)	ABCH	32.5±1.6
fcc(100)	(10×10×100)	ABCH	24.0±1.6
bcc(110)	(14×10×100)	ABCH	24.6±1.4
fcc(110)	(8×12×100)	ABCH	19.3±2.2
bcc(111)	(14×8×120)	ABCH	25.6±2.0
bcc(100)	(10×10×100)	Pair	30.8±7.0
bcc(110)	(14×10×100)	Pair	22.6±4.0
bcc(111)	(14×8×120)	Pair	23.1±3.6
bcc(100)	(10×10×100)	MH(SA)^2	45.8±3.8
bcc(110)	(14×10×100)	MH(SA)^2	33.5±1.0
bcc(111)	(14×8×120)	MH(SA)^2	31.8±1.8

D. Kinetic coefficients

The preparation of solid-liquid systems for the calculation of μ follows the approach described by us previously.[13] Solid-liquid coexisting MD cells with roughly 20% solid (liquid) for melting (growth), corresponding to different orientations of the fcc and bcc solid-liquid interface, are used for calculating μ. The orientations for each of these cells are listed in Table II. The geometries of these different cells are denoted as follows. For each cell (hkl) refers to the orientation of the solid-liquid interfaces. For the fcc(001) orientation, labeled as (10×10×100), the cell dimensions are 10 fcc nearest-neighbor spacings in length along the *x* and *y* (fcc $[1\bar{1}0]$ and $[110]$) directions parallel to the interface and, prior to melting, the initially crystalline cell contains 100 layers along the normal direction *z*. The fcc(110) orientation, labeled as (8×10×120), has dimensions of 8 times the fcc lattice constant along *x* ($[001]$), 10 times the nearest-neighbor distance along *y* ($[1\bar{1}0]$), and 120 initially crystalline layers in *z*. For the bcc(001) orientation, labeled (10×10×100), the cell is constructed with periodic lengths that are ten lattice constants along *x* and *y* [bcc (100), and (010) respectively], and contains 100 initially crystalline layers along *z*. The simulation cell for bcc(110), labeled as (14×10×100), is chosen to have $7\sqrt{2}$ lattice constants along *x* [bcc $(1\bar{1}0)$ direction] and 10 lattice constants along *y* [the bcc (001) direction], with 100 crystalline layers in *z*. Finally, the bcc(111) cell, labeled as (14×8×120), is $7\sqrt{2}$ lattice constants in *x* $(\bar{1}10)$, $4\sqrt{6}$ lattice constants along *y* $(\bar{1}\bar{1}2)$, and 120 crystal layers along *z*.

For the calculation of the kinetic coefficients, we use the free solidification method described in detail in our previous paper.[13] In this method, for a given undercooling, the system was simulated by employing Andersen-Parinello-Rahman[47–50] and Nosé-Hoover[51,52] dynamics, and the interface velocity V can be readily extracted through the slope of volume or energy versus time. In all the simulations for μ, only the length normal to the interface is allowed to change. The initial states for these coexisting solid and liquid phases were prepared as described in detail in previous work.[13] For

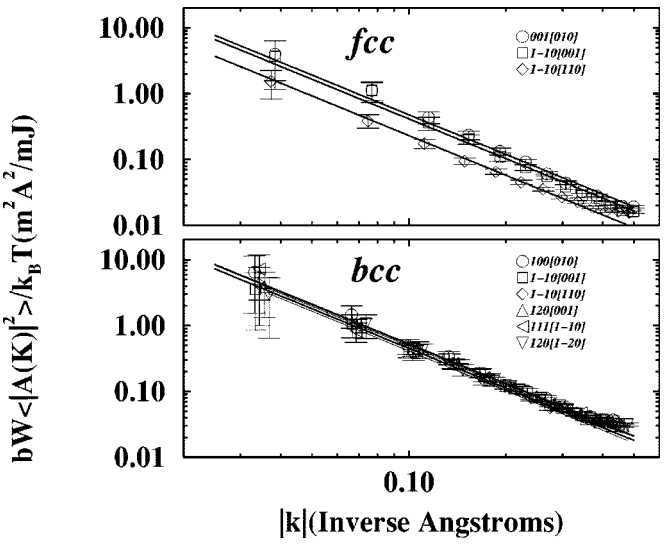

FIG. 1. Equilibrium fluctuation spectra $bW\langle A(k)^2\rangle/k_BT$, plotted on a log-log scale vs wave number k for both fcc (upper panel) and bcc (lower panel) Fe using the ABCH potential. The solid lines indicate the theoretical slope of k^{-2}. Error bars represent estimated standard statistical uncertainties.

each undercooling, four different uncorrelated configurations are chosen (obtained from equilibration runs spaced 50 ps apart) as the starting configurations for subsequent computer simulations of melting or growth and the total run time for each structure/orientation was ≈ 1 ns.

III. INTERFACIAL FREE ENERGIES

Results for the solid-liquid interfacial free energies in fcc and bcc Fe have been reported in Ref. 36. Here we briefly summarize the findings. Figure 1 is a log-log plot of $bW\langle|A(k)|^2\rangle/k_BT$ versus wave number k derived from the MD simulations for both fcc (upper panel) and bcc (lower panel) Fe using the ABCH potential. Error bars represent standard statistical uncertainties, estimated according to the following formula for the variance in the mean value of $\langle|A(k)|^2\rangle$, derived from the property that $\langle|A(k)|^2\rangle$ obeys Gaussian statistics: $\sigma^2=2[(bW/k_BT)\times\langle|A(k)|^2\rangle]^2\tau_c(k)/t_{run}$.[53] The correlation times $\tau_c(k)$ were calculated by integrating over time the autocorrection functions $\langle A(k,t)A(k,0)\rangle$ calculated from the simulations. The solid lines in Fig. 1 correspond to a fit to the data of the theoretical $1/k^2$ form. For each orientation, the theoretical prediction of Eq. (3) is seen to hold well within the statistical error bars for both phases over a wide range of k values. Similar results are obtained for the effective pair and MH(SA)^2 potential. As has been found in previous simulations, at the highest wave numbers, where the fluctuation wavelengths approach atomic dimensions, deviations from the predictions of Eq. (3) are observed. The offset of the curves from one another in Fig. 1 reflects the anisotropy in stiffness. Lower anisotropy for bcc is evident, as will be discussed further below.

The average solid-liquid interfacial free energies γ_0, and anisotropy parameters ϵ_1 and ϵ_2 (see Ref. 36) are listed in Table III. From the average values, one can see that the bcc solid-liquid interface has significantly lower interfacial free energies than fcc for both the ABCH and effective pair potentials. For the ABCH potential, the average interfacial free energy is about 206 mJ/m^2 for the bcc solid-melt interface, which is about 0.6 times smaller than the 319 mJ/m^2 found for the fcc interface. For the effective pair potential, the average interfacial free energy is 311 mJ/m^2 for fcc and 221 mJ/m^2 for bcc. Since the latent heats are similar for the bcc and fcc phases of a given EAM potential, the lower value of γ for the bcc phase implies a lower Turnbull coefficient. As described in Ref. 36, the lower Turnbull coefficient for bcc relative to that in the fcc phase is consistent with a poly-tetrahedral model of the solid-liquid interface structure,[54–56] computer simulations of nucleation in the Lennard-Jones system,[34] a direct computation of γ in the $1/r^6$ system,[57] and a numerical study of nucleation in weakly charged colloidal spheres.[58] In several experiments,[29,31,33,37,59] nucleation of the bcc phase was found at high undercooling even though the stable solid phase is fcc. Again the appearance of the bcc phase was successfully explained by assuming a smaller Turnbull coefficient for bcc relative to fcc.

The present results show that the effective pair and many-body form of the ABCH model give very similar interfacial free energy and anisotropy parameters, which implies that many-body interactions play a relatively minor role in determining equilibrium solid-liquid interface properties. In a recent MD simulation, the solid-liquid interface structures for both EAM Au and the LJ system were studied[60] and very similar interface structures were found. Also, in an MD simulation of the structure of the nickel crystal-melt interface,[61] it was found that the EAM potential produces a similar interface structure as that obtained by the LJ pair potential.[62] Both the EAM potential for Ni and the LJ potential yield a similar layer spacing and density change across

TABLE III. Calculated average interfacial free energy and anisotropy parameters for the fcc and bcc structures based upon the ABCH, MH(SA)^2, and ABCH effective-pair (Pair) potentials.

Crystal	Potential	α	γ_0 (mJ/m^2)	ϵ_1 (%)	ϵ_2 (%)	$\frac{\gamma_{100}-\gamma_{110}}{2\gamma_0}$ (%)	$\frac{\gamma_{100}-\gamma_{111}}{2\gamma_0}$ (%)
bcc	ABCH	0.32±0.02	206±10	1.6±0.12	−0.04±0.28	0.4±0.4	0.5±0.4
bcc	Pair	0.29±0.02	221±14	1.3±0.18	0.26±0.28	0.5±0.5	0.4±0.6
bcc	MH(SA)^2	0.36±0.02	175±11	3.3±0.18	0.24±0.32	1.0±0.6	1.0±0.2
fcc	ABCH	0.55±0.02	319±12	11.7±0.12	−0.17±0.28	2.8±0.4	3.9±0.4
fcc	Pair	0.50±0.02	311±14	10.0±0.14	−0.17±0.26	3.9±0.4	3.4±0.5

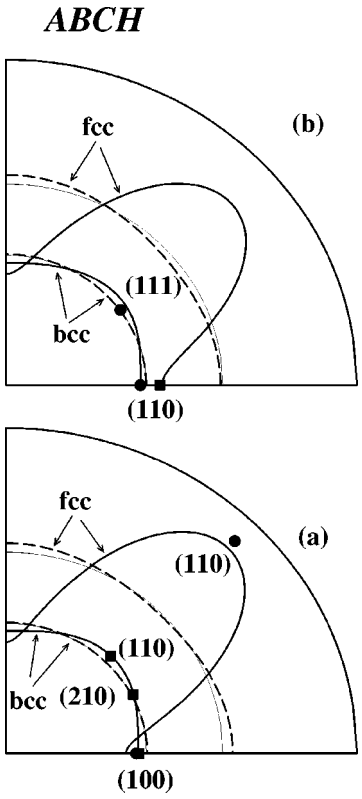

FIG. 2. Interfacial stiffness (solid line) and interfacial free energy (dash line) vs orientation predicted by the ABCH potential, for interfaces with normals in (a) the (001) plane and (b) the $(1\bar{1}0)$ plane. The full orientation dependence was generated from an expansion of the interfacial energy in terms of cubic harmonics. In (a), the orientation is characterized by the rotation angle about the [001] direction, with the (100) interface defining $\theta=0$. For (b), the (110) interface defines $\theta=0$. Points indicate the value of the stiffness obtained directly from MD simulations of the interface height fluctuations. The dotted line lying close to the free energy curve is the contour defined by $\gamma(n)=\gamma_0$.

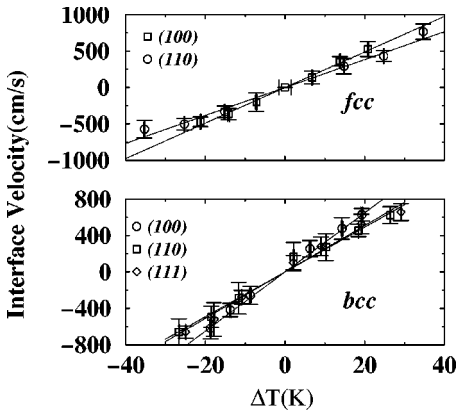

FIG. 3. Velocities of solid-liquid interfaces as a function of ΔT calculated using the ABCH potential for both fcc (upper panel) and bcc (lower panel). The error bars denote standard errors on the mean values of the measured velocities derived from the four independent simulations and solid lines correspond to least-squares fits to the data.

the interface. The situation for the solid-liquid interface is quite different from that for solid-vapor and liquid-vapor interfaces where many-body interactions are required to correctly reproduce effects associated with reduced coordination.[44,60] Reduced coordinations, or lower electron density, in the EAM model will enhance the strength of the effective bond and the enhancement of bond strength will change locally the atom density. Thus, liquid-vapor interfaces in the EAM model usually exhibit a peak in the atomic density, which is absent in the pairwise LJ system. For solid-liquid interfaces, the difference in atomic coordination is small across the phase boundary and it is perhaps not surprising that the EAM model and effective pair potential predict similar interface structures and properties.

Another important feature of the present results is the fact that the bcc phase has a significantly lower anisotropy of the interfacial free energy than fcc. The anisotropy parameters ϵ_1 and ϵ_2 listed in Table III are almost one order of magnitude smaller for bcc than those for fcc. To make the anisotropy more clear, in Fig. 2 we have plotted the stiffness (solid lines) and interfacial free energy (dashed lines) as a function of orientation in both the (100) and (110) planes. Here we use the cubic harmonic expansion for $\gamma(n)$ given in Ref. 36. Also shown are the data points for the stiffness obtained directly from fits of the MD height fluctuation spectra. As is made clear in this figure, the interfacial free energy plot for bcc is almost identical to a circle, indicating a nearly isotropic γ, while there is a clear deviation from a circle for the case of fcc. Also, as mentioned above, the stiffness is one order of magnitude more anisotropic than γ and this can be very clearly seen in the figure by comparing the solid and dashed lines.

Although only a few experiments have attempted to measure the anisotropy in γ, the lower anisotropy for bcc relative to that of fcc found here is consistent with results from transparent organic materials. In succinonitrile, a bcc structure, the anisotropy is one order of magnitude lower than the fcc material pivalic acid.[63] In addition, the low anisotropy in bcc may help to explain the observation from experimental studies of Fe and Fe alloys that solidification rates of the metastable bcc phase are much slower than those of the stable fcc structure (see the following section).

IV. THE KINETIC COEFFICIENT

Interface velocities V vs ΔT ($\Delta T=T-T_m$) for the bcc(100), bcc(110), and bcc(111) interfaces calculated with the ABCH potential, are shown in Fig. 3 (lower panel). As discussed previously, V is calculated from the change of the total volume accompanying melting/solidification and a knowledge of the equilibrium atomic volumes in the solid and liquid phases. The linear relationship $V=\mu\Delta T$ is seen to hold fairly well over the range of ΔT considered. Additionally, the results are found to be highly symmetric with respect to melting and growth. In Fig. 3 error bars denote estimated uncertainties (standard errors) in the mean value of V, obtained from the variance of the interface velocities derived separately from each of four independent simulations for a given ΔT. The kinetic coefficient (μ) is obtained by a

least-squares fit of the V vs ΔT data. For bcc Fe modeled with the ABCH potential, the resulting values of μ are 32.5 ± 1.6 cm/s K, 24.6 ± 1.4 cm/s K, and 25.6 ± 2.0 cm/s K for the (100), (110), and (111) orientations, respectively. The kinetic coefficient for (100) is thus largest, while the μ for (110) and (111) are close in magnitude. The anisotropies μ_{100}/μ_{110} and μ_{100}/μ_{111} are 1.32 ± 0.06 and 1.27 ± 0.07, respectively. To the best of our knowledge, the only previous MD calculation of μ for bcc was that for the (100) orientation of Na by Tymczak and Ray,[23,24] and therefore the present calculation is the first to compute the kinetic anisotropy for a bcc system.

Figure 3 (upper panel) shows the interface velocity vs ΔT for the fcc(100) and fcc(110) interfaces calculated using again the ABCH potential. μ is calculated to be 24.0 ± 1.6 cm/s K and 19.3 ± 2.2 cm/s K for the (100) and (110) growth directions, respectively. For fcc Fe, the kinetic anisotropies are consistent with the previous results for other fcc metals, namely, $\mu_{100}>\mu_{110}$ and $\mu_{100}/\mu_{110}=1.24\pm0.11$. Comparing with the μ obtained for bcc, we find that μ of fcc(100) is 0.74 times smaller than bcc(100).

We have repeated the same calculation for bcc interfaces employing instead the effective pair potential. Here the values $\mu_{100}=30.8\pm7.0$, $\mu_{110}=22.6\pm4.0$, and $\mu_{111}=23.1\pm3.6$ were obtained and the anisotropies μ_{100}/μ_{110} and μ_{100}/μ_{111} are 1.36 ± 0.21 and 1.33 ± 0.21, respectively. One can see that nearly identical anisotropies and magnitudes of μ are obtained with the effective-pair and many-body potential forms of the ABCH potential.

To further check the anisotropy in μ for the bcc phase, the same simulations were also performed using the more accurate MH(SA)^2 potential and μ was found to be 45.8 ± 3.8, 33.5 ± 1.0, and 31.8 ± 1.8 for the (100), (110), and (111) interfaces, respectively. Interestingly, although the MH(SA)^2 and ABCH potentials have substantially different forms, the anisotropy results are similar, namely, $\mu_{100}/\mu_{110}=1.37$ (±0.065) and $\mu_{100}/\mu_{111}=1.44(\pm0.070)$.

For all three potentials, the kinetic anisotropy is found to be approximately $\mu_{100}/\mu_{110}\sim1.35$ and $\mu_{100}/\mu_{111}\sim1.35$ for bcc Fe, in the order of $\mu_{100}>\mu_{110}\sim\mu_{111}$, which is independent of the detailed form of the potentials. Interestingly, the kinetic anisotropies derived for bcc Fe are very similar to those for fcc Fe and other fcc metals considered previously.[13,20–22] Furthermore, for all the models of Fe considered, μ for the bcc phase is found to be larger than for fcc.

The data in Fig. 3 [as well as that obtained with the effective pair and MH(SA)^2 potentials] feature highly symmetric results for melting and growth kinetics in the regime of low undercoolings explored in this work, which is in agreement with our earlier study of Ni (Ref. 13) and previous simulation results for the Lennard-Jones system.[17,18] This feature of the results is interesting in light of the large asymmetry between melting and growth kinetics derived for Au by Celestini and Debierre[22] using a ''glue'' potential of the form given by Eq. (1). Possible reasons for this discrepancy between the results for Au and those derived for Ni, Fe, and the LJ system were discussed by us previously.[13]

V. DISCUSSION

The present MD results yield the following kinetic anisotropy values for the bcc phase: $\mu_{100}/\mu_{110}\sim1.35$ and $\mu_{100}/\mu_{111}\sim1.35$. The ordering of μ with crystallographic orientation, namely $\mu_{100}>\mu_{110}\sim\mu_{111}$, is similar to the fcc Fe result obtained here, as well as all previous MD results for fcc-based systems. It has been pointed out previously by several authors[13,21,22,62] that this ordering is inconsistent with the commonly suggested scaling of the kinetic coefficient with crystalline interplanar spacing d_{hkl} for fcc.

An alternative framework for understanding the origin of μ anisotropy is offered by the kinetic DFT formulation of Mikheev and Chernov.[64] It has been shown that the Mikheev and Chernov model can provide reasonable estimates of the anisotropy for fcc materials.[13] In the kinetic DFT formulation of Mikheev and Chernov,[64] it is assumed that isothermal solid-liquid interface velocities are governed by the rate of propagation of crystalline ''density waves'' in advance of the moving solid-liquid interface. The model yields the following expression for the kinetic coefficient:

$$\mu=\frac{L}{k_B T_M^2}\frac{S(G_1)\xi_b}{\tau(G_1)A_s}. \tag{4}$$

$S(G_1)$ is the structure factor evaluated at the magnitude of the minimal reciprocal-lattice vector of the crystal, G_1, i.e., the first main peak in $S(k)$. $\tau(G_1)$ is the relaxation time of the liquid, which can be determined experimentally from the inverse half-width of the dynamical structure factor $S(k=G_1,\omega)$. Also in Eq. (4), ξ_b is the correlation length in the liquid, defined as the inverse half-width of $S(k)$ evaluated at the main peak and A_s is a factor governing the anisotropy of μ and is given by

$$A_s=\sum_{|\mathbf{G}|=\mathbf{G}_1}\frac{\xi_b}{\xi_{\mathbf{G}}}. \tag{5}$$

Here $\xi_{\mathbf{G}}$ represents the effective width of the Fourier transform of the number density profile, $\eta_{\mathbf{G}}$, across the solid-liquid interface (a more precise definition of $\eta_{\mathbf{G}}$ will be given below). The sum in the above expression is over all the first-neighbor reciprocal lattice vectors (8 for fcc and 12 for bcc). The effective widths $\xi_{\mathbf{G}}$ are unknown quantities, and thus the Mikheev and Chernov model relies on an analytic approximation, derived in an earlier paper,[65] for the density profile of a liquid in contact with a solid whose underlying periodicity is described by any given set of reciprocal lattice vectors. For pure fcc metals, the approximate relationship for the effective widths is given by $\xi_{\mathbf{G}}=\xi_b\cos\theta$, where θ is the angle between the vector $\mathbf{G}$ and the interface normal. The remaining unknowns in the Mikheev-Chernov expression, $S(G_1)$, ξ_b, and τ, are also not known for most liquid metals. For these quantities Mikheev and Chernov use results from the well-studied hard-sphere system.

With the hard-sphere approximation and the approximate form for the interface widths, the Mikheev and Chernov model predicts $\mu_{100}\approx10.0$ for fcc Fe, which is 2.5 times smaller than the MD results. The magnitude of μ predicted

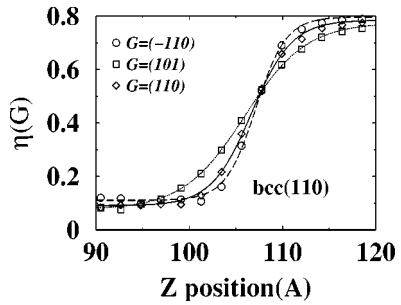

FIG. 4. The $\eta_{\mathbf{G}}$ number density profiles for the bcc solid-liquid interface using the ABCH potential. The profiles are shown as a function of position along the interface normal. Results from all the nonequivalent **G** vectors from the minimal set are shown.

by the Mikheev and Chernov model was also found to be too low for LJ, Ni, and Pb.[3,13,14] How to improve/modify the Mikheev and Chernov model is a subject of work in progress. However, for the purposes of the present discussion, we will continue to use the theory as a way of understanding the trends observed in the MD results. For example, the ratios μ_{100}/μ_{110} and μ_{100}/μ_{111} can be found by evaluating only the factors A_s in Eq. (4). Furthermore, the growth rate of the fcc phase relative to the bcc structure can be determined from the following ratio:

$$\frac{\mu^{fcc}}{\mu^{bcc}} = \frac{L^{fcc}(T_M^{bcc})^{3/2}}{L^{bcc}(T_M^{fcc})^{3/2}} \frac{\xi_b^{fcc} A_s^{bcc}}{\xi_b^{bcc} A_s^{fcc}}, \tag{6}$$

where the exponent of 3/2 on the temperature arises by assuming that relaxtion times in the liquid are proportional to the thermal velocity of atoms, which in turn varies as $T_M^{1/2}$. Also, the small variation of $S(G_1)$ with temperature has been neglected. From Eq. (6) it is clear that the only unknowns in the ratio of μ's are again the A_s terms. Since the A_s coefficients also determine the kinetic anisotropy, it is important to compute A_s as precisely as possible. Therefore, rather than using the approximation $\xi_{\mathbf{G}} = \xi_b \cos\theta$ to obtain the widths appearing in Eq. (5), we instead evaluate $\xi_{\mathbf{G}}$, and hence A_s, directly from MD simulations of equilibrium solid-liquid systems.

In the Mikheev and Chernov formulation, anisotropy in μ originates from the geometric projection upon the growth direction of density waves with wave vectors $\mathbf{G}_1$. The density profile $\eta_{\mathbf{G}}$ along the interface normal direction increases sharply as the boundary is traversed from the liquid phase to the solid and the width of these density profiles determines the anisotropy factors A_s. To calculate $\eta_{\mathbf{G}}$ from MD simulations, we use a technique similar to the one developed by Chen, Barnett, and Landman.[61] The system is first divided into layers normal to the interface where the spacing of the layers corresponds to the layer spacing in the solid. For each layer, we calculate $\eta_{\mathbf{G}}(l)$ according to the following:

$$\eta_{\mathbf{G}}(l) = \left\langle \frac{1}{N_l} \sum_{i \in l}^{N_l} \exp(i\mathbf{G}\cdot\mathbf{r}) \right\rangle, \tag{7}$$

where N_l is the number of atoms in lth layer and the angular brackets denote an average over configurations. We have modified the method by Chen, Barnett, and Landman in two ways. First, in the present calculation, the average is only over those configurations in which the length of the solid region and the pressure of the system are close to the average value. Second, for each configuration, the lower interface was always shifted to a fixed position. The above two modifications help eliminate the effects due to fluctuations in the interface position over the course of an MD run. The modifications were important since the deviation in the boundary position due to fluctuations was found to be on the order of interface width itself.

Figure 4 shows the $\eta_{\mathbf{G}}$ profile for the bcc phase of Fe (ABCH potential) where the interface normal is the (110) direction. The three curves in Fig. 4 represent the entire set of nonequivalent $\mathbf{G}_1$ vectors. It is clear that the effective width of the η_{G} profile depends on the orientation of the $\mathbf{G}_1$ vector with respect to the interface normal and the profiles are sharpest for those orientations with the smallest values of the angle θ. In Fig. 5, $\eta_{\mathbf{G}}$ curves are plotted for the case MH(SA)^2 Fe in the bcc phase. Similar features are obtained as in Fig. 4. The $\eta_{\mathbf{G}}$ computations were also performed for the fcc structure of Fe and the results were used to determine the anisotropy factors and the ratio of μ's.

To calculate A_s, the $\eta_{\mathbf{G}}$ profiles were fit to a tanh form and the widths $\xi_{\mathbf{G}}$ were extracted. The anisotropy factor A_s was then calculated through Eq. (5). In Table IV, we list the kinetic anisotropy calculated from the Mikheev and Chernov model using the A_s obtained directly from MD simulation. The calculated anisotropy is $\mu_{100}/\mu_{110} = 1.08$ and $\mu_{100}/\mu_{111} = 1.14$ for the ABCH bcc phase. The anisotropy

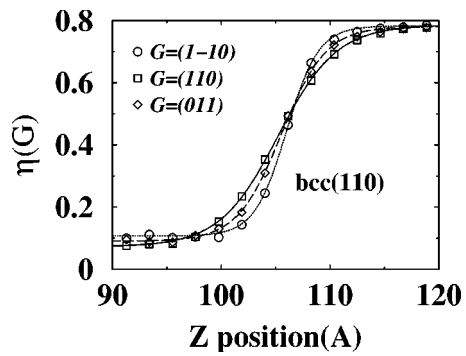

FIG. 5. The $\eta_{\mathbf{G}}$ profiles for the bcc solid-liquid interface using the MH(SA)^2 potential.

TABLE IV. The bcc anisotropy of the kinetic coefficient calculated by MD simulation and by the Mikheev-Chernov model.

	Mikheev-Chernov	MD	Potential
μ_{100}/μ_{110}	1.08	1.32 ± 0.06	ABCH
μ_{100}/μ_{111}	1.14	1.27 ± 0.07	ABCH
μ_{100}/μ_{110}	1.14	1.37 ± 0.07	MH(SA)^2
μ_{100}/μ_{111}	1.23	1.44 ± 0.07	MH(SA)^2

predicted by the Mikheev and Chernov model is consistently lower than the MD results. However, the model does reproduce the correct ordering of the kinetic coefficient, i.e., $\mu_{100} > \mu_{110} \sim \mu_{111}$, and, as mentioned above, this result cannot be explained by the ratio d spacings in the bcc crystal structure.

The values of the A_s coefficients obtained from MD simulation can also be used to compute the crystallization rate of the bcc phase relative to that of the fcc phase. Evaluating Eq. (6), we find that the Mikheev and Chernov model predicts roughly equal crystallization rates for the fcc and bcc phases. Recall, the MD results show that bcc is slightly faster than fcc (Table II). Using an electromagnetic levitation technique, Zambon *et al.*[29] measured the dendrite growth velocity as a function of undercooling for various compositions of Fe-Ni alloys. The authors found that below a critical undercooling, which depends on alloy composition, the metastable bcc phase, rather than fcc, is formed and subsequently solidifies. Therefore a direct experimental comparison between the growth rates of fcc vs bcc was possible. The kinetic results were found to be in good agreement with a dendrite growth model due to Boettinger *et al.*[66] only if the kinetic coefficient of the bcc was assumed to be a factor of 4 lower than that of fcc. The much lower value of μ for the bcc structure contradicts both the MD results for pure Fe given in Table II and the prediction of the Mikheev-Chernov growth model. There is, however, an alternative explanation for the sluggish growth kinetics of the bcc phase observed in experiment. The generally accepted theoretical model of dendrite growth is the so-called microscopic solvability theory.[67,68] Microscopic solvability predicts that the operating point of a dendrite, i.e., its growth velocity and tip radius, are determined by the anisotropy in the solid-liquid interfacial free energy and smaller values of the anisotropy lead to slower growth rates. Since the anisotropy in γ was not known, Zambon *et al.* did not consider this effect. However, the MD results for γ presented in Fig. 2 demonstrate that the anisotropy of the bcc phase is in fact considerably less than that of the fcc phase. A rigorous comparison between theory and experiment requires a full phase field calculation of dendrite growth as was done by Bragard *et al.*[25] for pure Ni, but the small bcc anisotropy in γ found in the present study offers a plausible explanation for the slow growth rates of the bcc phase seen in Fe-Ni alloys.

Finally, the Mikheev and Chernov model can also be used to predict the ratio of kinetic coefficients for the various Fe potentials. Using the latent heat, melting point, structure factor and A_s, we also calculated the ratio of μ_{100} for the MH(SA)^2 and ABCH potentials. We find that μ_{100} for the MH(SA)^2 potential is 1.16 times larger than that for the ABCH potential, which is in reasonable agreement with MD free solidification results.

VI. SUMMARY

In this paper, we have calculated the solid-liquid interfacial free energy and mobility in pure Fe where two separate EAM potentials and an effective-pair potential were used. In addition to a stable bcc phase, the potential due to ABCH produces a metastable fcc phase with a melting point that is only slightly lower. Thus a direct comparison of interface properties for the bcc and fcc structures can be made using the same interatomic potential. We find that the kinetic coefficient of bcc is larger than fcc, but the associated kinetic anisotropies are quite similar. The calculated anisotropies are $\mu_{100}/\mu_{110} \sim 1.35$ and $\mu_{100}/\mu_{111} \sim 1.35$ for bcc. The present results for kinetic anisotropies are similar to most fcc solid-liquid interfaces studied previously. MD results for the kinetic anisotropy are higher than, but in reasonable agreement with the Mikheev-Chernov growth model.

ACKNOWLEDGMENTS

This research was supported by the U.S. Department of Energy, Office of Basic Energy Sciences, under Contract No. DE-FG02-01ER45910, as well as the DOE Computational Materials Science Network program. Use was made of resources at the National Energy Research Scientific Computing Center, which was supported by the Office of Science of the Department of Energy under Contract No. DE-AC03-76SF00098. Sandia is a multiprogram national laboratory operated by Sandia Corporation, a Lockheed Martin Company, for the United States Department of Energy under Contract No. DE-AC04-94AL8500. We are grateful for numerous helpful discussions with Professor Alain Karma.

*Permanent address: Institute of Solid State Physics, Academia Sinica, 230031-Hefei, China.

[1] W.J. Boettinger, S.R. Coriell, A.L. Greer, A. Karma, W. Kurz, M. Rappaz, and R. Trivedi, Acta Mater. **48**, 43 (2000).
[2] M.E. Glicksman and R.J. Schaefer, J. Cryst. Growth **1**, 297 (1967).
[3] G.H. Rodway and J.D. Hunt, J. Cryst. Growth **112**, 554 (1991).
[4] J.J. Hoyt, M. Asta, and A. Karma, Mater. Sci. Eng., R. **41**, 121 (2003).
[5] J.Q. Broughton and G.H. Gilmer, J. Chem. Phys. **84**, 5749 (1986).
[6] R.L. Davidchack and B.B. Laird, Phys. Rev. Lett. **85**, 4751 (2000).
[7] R.L. Davidchack and B.B. Laird, J. Chem. Phys. **118**, 7651 (2003).
[8] J.J. Hoyt, M. Asta, and A. Karma, Phys. Rev. Lett. **86**, 5530 (2001).
[9] J.J. Hoyt and M. Asta, Phys. Rev. B **65**, 214106 (2002).
[10] J.R. Morris, Phys. Rev. B **66**, 144104 (2002).
[11] M. Asta, J.J. Hoyt, and A. Karma, Phys. Rev. B **66**, 100101(R) (2002).
[12] J.R. Morris and X.Y. Song, J. Chem. Phys. **119**, 3920 (2003).
[13] D.Y. Sun, M. Asta, and J.J. Hoyt, Phys. Rev. B **69**, 024108 (2004).
[14] J.Q. Broughton, G.H. Gilmer, and K.A. Jackson, Phys. Rev. Lett. **49**, 1496 (1982).
[15] E. Burke, J.Q. Broughton, and G.H. Gilmer, J. Chem. Phys. **89**, 1030 (1988).
[16] H.L. Tepper and W.J. Briels, J. Cryst. Growth **230**, 270 (2001).
[17] H.L. Tepper and W.J. Briels, J. Chem. Phys. **115**, 9434 (2001).
[18] H.L. Tepper and W.J. Briels, J. Chem. Phys. **116**, 5186 (2002).
[19] W.J. Briels and H.L. Tepper, Phys. Rev. Lett. **79**, 5074 (1997).
[20] J.J. Hoyt, B. Sadigh, M. Asta, and S.M. Foiles, Acta Mater. **47**,

3181 (1999).
[21] J.J. Hoyt, M. Asta, and A. Karma, Interface Sci. **10**, 149 (2002).
[22] F. Celestini and J.-M. Debierre, Phys. Rev. E **65**, 041605 (2002).
[23] C.J. Tymczak and J.R. Ray, Phys. Rev. Lett. **64**, 1278 (1990).
[24] C.J. Tymczak and J.R. Ray, J. Chem. Phys. **92**, 7520 (1990).
[25] J. Bragard, A. Karma, Y.H. Lee, and M. Plapp, Interface Sci. **10**, 121 (2002).
[26] R.E. Cech, Trans. AIME **206**, 535 (1956).
[27] G. Ghosh, Mater. Sci. Eng., A **189**, 277 (1994).
[28] T. Volkmann, W. Löser, and D.M. Herlach, Metall. Mater. Trans. A **28A**, 453 (1997).
[29] A. Zambon, B. Badan, K. Eckler, F. Gärtner, A.F. Norman, A.L. Greer, D.M. Herlach, and E. Ramous, Acta Mater. **46**, 4657 (1998).
[30] M. Li, Z. Lin, G. Song, G. Yang, and Y. Zhou, Mater. Sci. Eng., A **268**, 90 (1999).
[31] D.M. Herlach, J. Phys.: Condens. Matter **13**, 7737 (2001).
[32] A.L. Greer and I.T. Walker, J. Non-Cryst. Solids **317**, 78 (2003).
[33] C. Notthoff, B. Feuerbacker, H. Franz, D.M. Herlach, and D. Holland-Moritz, Phys. Rev. Lett. **86**, 1038 (2001).
[34] P.R. ten Wolde, M.J. Ruiz-Montero, and D. Frenkel, Phys. Rev. Lett. **75**, 2714 (1995).
[35] Y.C. Shen and D.W. Oxtoby, Phys. Rev. Lett. **77**, 3585 (1996).
[36] D.Y. Sun, M. Asta, J.J. Hoyt, M.I. Mendelev, and D.J. Srolovitz, Phys. Rev. B **69**, 020102 (2004).
[37] K. Eckler, F. Gärtner, H. Assadi, A.F. Norman, A.L. Greer, and D.M. Herlach, Mater. Sci. Eng., A **226-228**, 410 (1997).
[38] G.J. Ackland, D.J. Bacon, A.F. Calder, and T. Harry, Philos. Mag. A **75**, 713 (1997).
[39] M.I. Mendelev, S. Han, D.J. Srolovitz, G.J. Ackland, D.Y. Sun, and M. Asta, Philos. Mag. **83**, 3977 (2003).
[40] A.T. Dinsdale, CALPHAD: Comput. Coupling Phase Diagrams Thermochem. **15**, 317 (1991).
[41] G. Ghosh and G.B. Olson, Acta Mater. **50**, 2655 (2002).
[42] C. Hausleitner and J. Hafner, J. Phys.: Condens. Matter **1**, 5243 (1989).
[43] Q. Williams, R. Jeanloz, J. Bass, B. Svendsen, and T.J. Ahrens, Science **235**, 181 (1987).
[44] A.E. Carlsson, Solid State Phys. **43**, 1 (1990).
[45] J.R. Morris, C.Z. Wang, K.M. Ho, and C.T. Chan, Phys. Rev. B **49**, 3109 (1994).
[46] *Smithells Metals Reference Book*, 7th ed., edited by E.A. Brandes and G. B. Brook (Butterworth-Heinemann, Oxford, 1992).
[47] H.C. Andersen, J. Chem. Phys. **72**, 2384 (1980).
[48] M. Parinello and A. Rahman, Phys. Rev. Lett. **45**, 1196 (1981).
[49] M. Parinello and A. Rahman, J. Appl. Phys. **52**, 7182 (1981).
[50] M. Parinello and A. Rahman, J. Chem. Phys. **76**, 2662 (1982).
[51] S. Nosé, J. Chem. Phys. **81**, 511 (1984); Mol. Phys. **52**, 255 (1984).
[52] W.G. Hoover, Phys. Rev. A **31**, 1695 (1985); **34**, 2499 (1986).
[53] M. P. Allen and D.J. Tildesley, *Computer Simulation of Liquids* (Clarendon Press, Oxford, 1993).
[54] F. Spaepen, Acta Metall. **23**, 729 (1975).
[55] F. Spaepen and R.B. Meyer, Scr. Metall. **10**, 257 (1976).
[56] C.V. Thompson, Ph.D. thesis, Harvard University, 1979.
[57] B.B. Laird (private communication).
[58] S. Auer and D. Frenkel, J. Phys.: Condens. Matter **14**, 7667 (2002).
[59] W. Löser, A. Garcia-Escorial, and B. Vinet, Int. J. Non-Equilib. Process. **11**, 87 (1998).
[60] O. Tomagnini, F. Ercolessi, S. Iarlori, F.D. Di Tolla, and E. Tosatti, Phys. Rev. Lett. **76**, 1118 (1996).
[61] E.T. Chen, R.N. Barnett, and U. Landman, Phys. Rev. B **40**, 924 (1989).
[62] H.E.A. Huitema, M.J. Vlot, and J.P. van der Eerden, J. Chem. Phys. **111**, 4714 (1999).
[63] M.E. Glicksman and N.B. Singh, J. Cryst. Growth **98**, 277 (1989).
[64] L.V. Mikheev and A.A. Chernov, J. Cryst. Growth **112**, 591 (1991).
[65] L.V. Mikheev and A.A. Chernov, Sov. Phys. JETP **65**, 971 (1987).
[66] W.J. Boettinger, S. R. Coriell, and R. Trivedi, in *Rapid Solidification Processing, Principles and Technologies IV*, edited by R. Mehrabian and P.A. Parrish (Claitor's, Baton Rouge, 1988), p. 13.
[67] J.S. Langer, in *Chance and Matter*, Proceedings of the Lectures on the Theory of Pattern Formation, edited by J. Souletie, J. Vannimenus, and R. Stora, Session 46 (North Holland, Amsterdam, 1987), p. 629.
[68] D. Kessler, J. Koplik, and H. Levine, Adv. Phys. **37**, 255 (1988).